73rd International Astronautical Congress (IAC) – Paris, France, 18-22 September 2022.
Copyright © 2022 by Mr. G. Di Domenico. Published by the IAF, with permission and released to the IAF to publish in all forms.

IAC-21,D4,1,1,x65902

STASIS: An Attitude Testbed for Hardware-in-the-Loop Simulations of Autonomous Guidance, Navigation, and Control Systems

Gianfranco Di Domenico[1], **Francesco Topputo**[2]

Dept. of Aerospace Science and Technology, Politecnico di Milano
Via Giuseppe La Masa 34, 20156, Milano, Italy

In the last decade, we assisted to a consistent growth of the space sector, mainly fueled by the increasing employment of CubeSat technology. CubeSats have allowed to significantly reduce both manufacturing and launch costs, enabling missions to be carried on even with lower budgets. In particular, missions targeting terrestrial orbits benefitted the most from the employment of smaller satellites; conversely, the growth of the deep-space sector lagged behind, notably because of the high costs related to on-ground operations. The ERC-funded EXTREMA (Engineering Extremely Rare Events in Astrodynamics for Deep-Space Missions in Autonomy) project aims to disrupt the current paradigm for deep-space missions by enabling CubeSats with autonomous guidance, navigation, and control capabilities. To do so, it builds on three fundamental research Pillars and aims to integrate their scientific outcomes in a hardware-in- the-loop experimental facility, the Orbital Simulation Hub (OSH). STASIS (SpacecrafT Attitude SImulation System) is an attitude testbed currently under development at the DART laboratory of Politecnico di Milano. Its goal is to faithfully reproduce the attitude dynamics of a space probe in deep space and support the hardware-in-the-loop simulations that will be carried on in the EXTREMA OSH. The system is based on an air-bearing spherical joint capable of compensating the gravitational force acting on the Earth with a supporting thin film of air, ensuring the quasi-frictionless motion of the overlying platform with three rotational degrees of freedom. On its top, STASIS hosts a FlatSat, an assembly integrating all the necessary subsystems to run the autonomous GNC algorithms developed within the EXTREMA Pillars, which performance and behavior are to be assessed. The paper will be structured as follows: in the first part, the functionalities of STASIS will be outlined; the challenges to face in order to achieve the fulfillment of the identified requirements will be introduced, including the balancing, powering, and estimation of the platform current state. In the second part, the current status of STASIS development will be described, detailing the employed systems and algorithms and highlighting the trade-offs that ultimately led to the design choices opted for. Finally, the last part will be focused on future scenarios, highlighting how STASIS – ergo, the OSH and EXTREMA itself – could act as a game-changing technology to pave the way towards fully autonomous interplanetary missions.

Introduction

The last years have seen the space sector experiencing a thriving growth. According to [1, 2], the number of space launches doubled from 2020 to 2021. The same trend is expected in 2022, with the number of launches as of July already exceeding the entire previous year. Furthermore, more than 300 are planned for 2023, confirming the involvement of a rising number of players in the space sector. A considerable role in this growth is represented by the significant decrease in access costs to space. Investments in the field and technological advances led to lower and lower budgets needed to carry on a space mission: in particular, CubeSats have enabled parties not backed up by huge capitals (as universities or smaller private companies) to space thanks to their low design, manufacturing, and launch costs. Furthermore, by relying on components-off-the-shelf (COTS), CubeSats also need less testing and validation procedures, cutting down costs and time-to-flight even more. It should be noted, however, that the space sector expansion was biased towards that part of space closer to the Earth. Indeed, only a tiny fraction of the total space launches targeted interplanetary orbits. Moreover, as longer durations characterize deep-space missions, the advantages brought by CubeSats technology are hindered by the extensive resources - both in terms of budget and human personnel - required to sustain the human-in-the-loop ground operations during multiple months or years. Moreover, no matter the available budget: ground slots for communications are scarce and are expected to saturate soon. In this framework, deep space is - and will

[1]PhD Student, gianfranco.didomenico@polimi.it
[2]Full Professor, francesco.topputo@polimi.it

Copyright © 2022 by Mr. G. Di Domenico. Published by the IAF, with permission and released to the IAF to publish in all forms.

be - a prerogative of a few more prominent stakeholders and agencies. The EXTREMA project (Engineering Extremely Rare Events in Astrodynamics for Deep-Space Missions in Autonomy) [3]aims to steer from such a future scenario by triggering a paradigm shift, enabling deep-space spacecraft with autonomous guidance, navigation, and control capabilities. The project has been awarded a five-year grant from the European Research Council and is planned to last until 2025.

- **Pillar I: Autonomous Navigation.** The first Pillar within EXTREMA focuses on the development of navigation algorithm to enable CubeSats to locate themselves in deep space in complete autonomy by exploiting the information in the surrounding environment.
- **Pillar II: Autonomous Guidance and Control.** The second Pillars aims to directly shift the current guidance paradigm. As of today, trajectory planning is performed on ground due to the limited computational resources available on board. Correction maneouvers have to be planned from ground too, employing a great amount resources in terms of time and human personnel. EXTREMA aims to develop lightweight and robust closed-loop guidance algorithms, expoiting the knowledge of the spacecraft position to compute a new trajectory according to a specific set of criterias to achieve the mission objectives in complete autonomy.
- **Pillar III: Autonomous Ballistic Capture.** The limited resources characterizing CubeSats systems could represent a bottleneck in achieving specific mission objectives as, for instance, expensive orbit inesertion maneouvers. Because of this, EXTREMA aims to further develop the autonomy of deep-space probes by engineering ballistic capture, exploiting the multi-body dynamics of the Solar System to remain in the proximity of the target body for a prolonged period of time.

The outcome of each Pillar is meant to be integrated into a series of experiments and, ultimately, brought together in the EXTREMA Simulation Hub (ESH) [4]: a hardware-in-the-loop testing facility that would allow testing integrated guidance, navigation and control (GNC) systems and algorithms (Figure 1). The experimental facility under construction in Politecnico di Milano's laboratories will integrate three different hardware-in-the-loop facilities under a comprehensive HIL simulation framework:

- **RETINA: Realistic Experimental faciliTy for vision-based NAvigation**. RETINA is an optical facility that will simulate the light pattern as received by the spacecraft optical camera through a set of lenses and screens. The output image will be employed for testing and validating optical navigation algorithms based on image processing of deep-space starfields.
- **ETHILE: EXTREMA THruster In the Loop Experiment**. ETHILE is a cold-gas thrust test bench that will mimic the thruster as employed by the spacecraft. In order to allow the simulation of multiple types of thrusters, a scaling framework based on dynamic similarity is employed to map the physical parameters of ETHILE to the ones of the target thruster [5].
- **STASIS: SpacecrafT Attitude SImulation System**. STASIS is an air-bearing platform used to simulate the attitude evolution of a spacecraft in deep space. STASIS will also host the board representing the on-board computer of the spacecraft and the set of attitude sensors and actuators to be employed on the spacecraft. It features a set of moving masses, a wireless power generation system, and a set of additional attitude actuators to compensate for the difference in inertial properties between the platform and the spacecraft.

In this paper, the design processes and outcomes related to the realization of STASIS will be described. In Section 1, STASIS will be introduced, along with the requirements of the integrated deep-space interplanetary transfer simulation; a high-level Functional Breakdown Structure (FBS) for STASIS will be outlined, and the main subsystems introduced. In Sections 2 to 4 the FBS will be detailed, and each one of the subsystems will be described. The design procedures and the associated chosen solutions of each subsystem will be explained. A high-level overview of the algorithms in development to guarantee the fulfillment of the platform requirements will be given. In the last part, future developments for STASIS will be outlined, and the potential of the platform - and, by projection, the ESH itself - will be discussed.

Copyright © 2022 by Mr. G. Di Domenico. Published by the IAF, with permission and released to the IAF to publish in all forms.

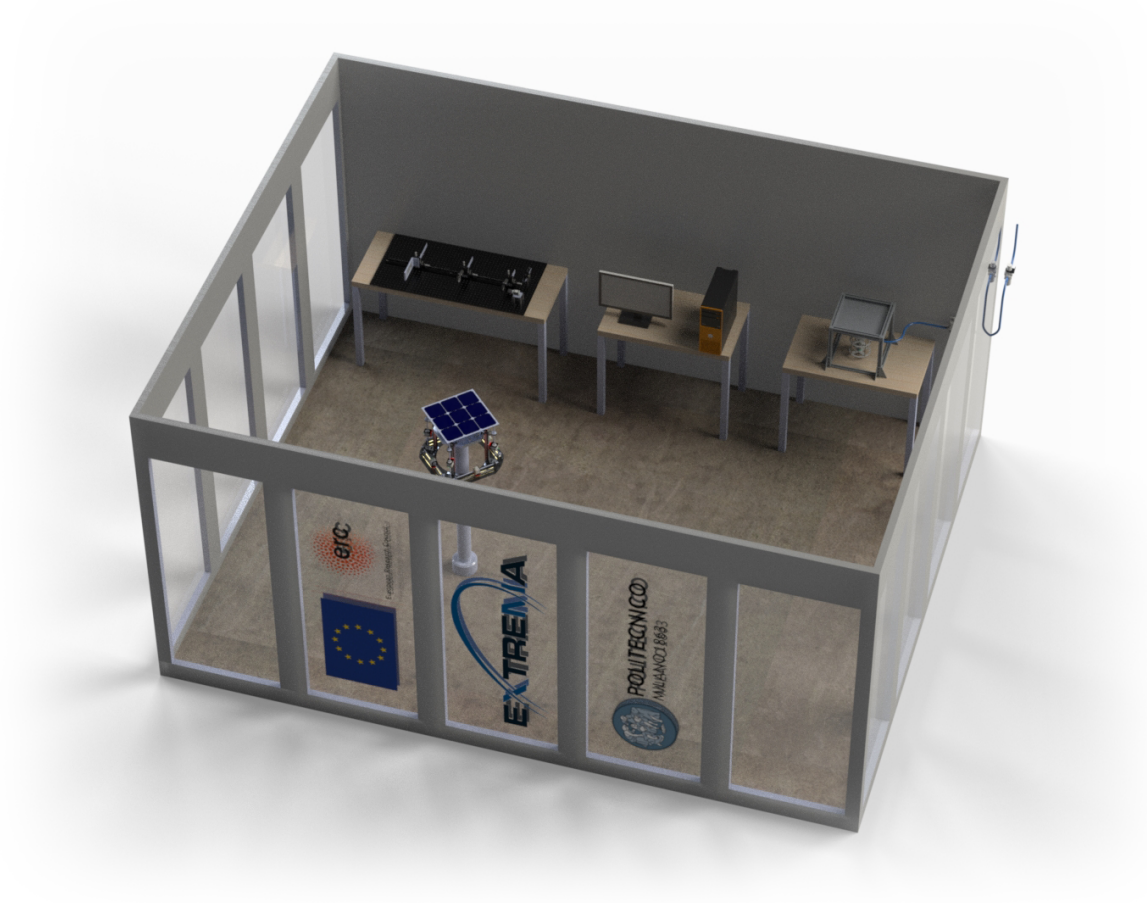

Fig. 1: Layout of the facilities in the ESH. RETINA: top-right corner; ETHILE: top-left corner; STASIS: in the middle.

1 STASIS: the attitude simulation platform

The main goal of the EXTREMA project is to ease the activities of design, verification, and validation of CubeSats' GNC systems for deep-space interplanetary missions. To achieve that, it plans to realize an integrated hardware-in-the-loop facility in which to test such systems and algorithms to navigate and steer the spacecraft in autonomy during interplanetary transfers.

1.1 Simulation scope and requirements identification

In industry, testing autonomous system usually relies heavily on on-field testing. This has been true, for istance, for automotive [6] and drones [7] applications. However, on-field testing for space systems is usually problematic, given the intrinsic differences between the Earth environment and the space one. Reference [8] gives a comprehensive overview the facilities designed to perform simulation of proximity maneouvers; facilities thought to simulate the deep-space environment are much difficult to find in literature. This is partially due to the fact that the involved characteristic times are longer, restricting the simulation to single mission phases or single subsystems. GNC for interplanetary transfers is usually characterized by a) interaction between multiple subsystems and domains, and b) extended transfer times. The ESH plans to address these as follows. For what concerns the interaction between multiple subsystems, a hardware-in-the-loop approach is conceived. Such approach relieves the computing units from the effort required to model the interaction between systems with diverse characteristic times and physical domains. The hub relies on real-world dynamics and a set of sensors to track the evolution of the systems and estimate their state. The second issue is instead

Copyright © 2022 by Mr. G. Di Domenico. Published by the IAF, with permission and released to the IAF to publish in all forms.

addressed with an accelerating approach relying on the dynamic similarity. A set of scaling parameters is employed to map the "target world" to the laboratory environment; the scaling parameters are conveniently adjusted, employing smaller acceleration factors during the most critical simulation phases (Figure 2) [9].

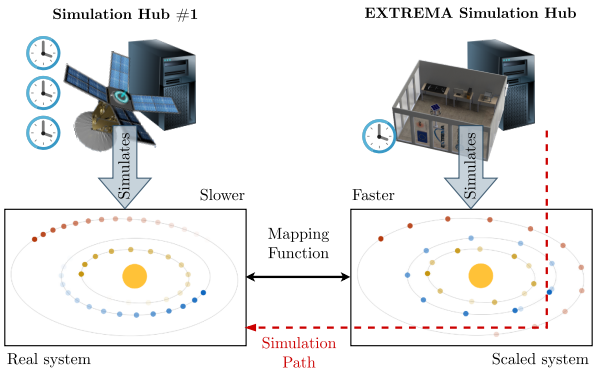

Fig. 2: Schematic of the acceleration approach employed in the ESH. Information on the target environment and systems are obtained by following the simulation path in reverse.

1.2 *Attitude evolution during an interplanetary transfer*

In order to identify the requirements of the attitude simulation platform, the attitude evolution of a typical spacecraft during an interplanetary transfer is here discussed. The closed-loop guidance approach envisioned in EXTREMA foresees the interplanetary transfer phase roughly divided in two phases:

a a cruising/reference tracking phase, in which the spacecraft actuates the thrust control as computed by the trajectory optimization algorithm

b a navigation/slew phase, in which the spacecraft performs a series of slew maneouvers to get optical information on its position in deep space and subsequently executes the navigation and trajectory computing routines.

From those, two different phases for attitude requirements identification can be defined. In the first phase, the spacecraft must adapt its orientation such that the thruster pointing direction is as close as possible to the nominal thrust vector direction as computed by the optimized orbital control profile. In the second phase, a sequence of slew maneouvers must be carried on, each one such that the target planet appears in the spacecraft camera's field of view (FOV) [10]. Then, the spacecraft must run the navigation and trajectory optimization algorithm and re-align its orientation before switching to phase one.
Additional phases could, of course, be envisioned, as desaturation maneouvers or antenna pointing for paylod and/or telemetry data relaying. Figure 3 shows a single simulation step as envisioned in the ESH. In the figure, the relationships and interaction between the different subsystems are explained. As the simulation must happen in real-time, it is paramount to ensure that all the operations within a single simulation step are executed before a single timestep of the orbital integrator. Such integrator should be designed accounting for the requirements of stability and real-timeness of the simulation. Implicit integrators - relying on the information of the system state on subsequent steps are not employable. Reference [9] details the choice of the integrator for the ESH.

1.3 *Reference spacecraft*

As the platform is thought to be as flexible as possible and to be able to simulate a number of different CubeSat configurations, there is no need to define a detailed FBS with associated requirements for the spacecraft to be simulated. However, at least a high-level functional breakdown structure of the spacecraft must be available. In this prelimiary design phase, has been thought as follows:

- an attitude control subsystem based on a set of 4 reaction wheels;
- an attitude sensing suite based on star tracker(s), gyroscope(s), and accelometer(s);
- an imaging subsystem, based on one or multiple optical cameras;
- an on-board computing suite based on a main on-board computer (OBC) and a subset of secondary boards (e.g., navigation image processing unit, thrust allocation unit, ...);
- a power generation system based on solar arrays;
- a high-efficiency, high-specific-impulse thruster (e.g., ion thruster), with associated sensor/integration units for spacecraft mass estimation;

The architecture of the reference spacecraft is chosen such that the minimum subsystems to perform closed-loop guidance during the interpolanetary transfer and remain close to the target by exploiting ballistic capture. Of course, the addition and simulation of additional subsystems could be properly integrated in the facility as needed.
According to the above list, for what concerns the attitude evolution of the spacecraft, the subsystems to integrate on STASIS should be an attitude control and

Copyright © 2022 by Mr. G. Di Domenico. Published by the IAF, with permission and released to the IAF to publish in all forms.

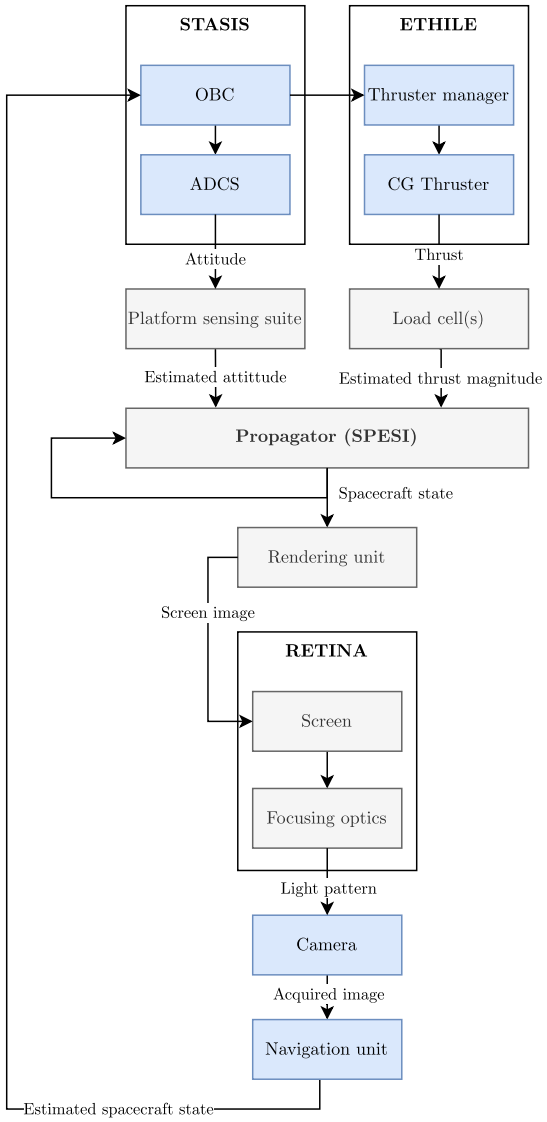

Fig. 3: Logical workflow of the ESH during the interplanetary transfer simulation

actuation subsystem (with a set of four reaction wheels) and an attitude estimation subsystem, with the proper sensors, algorithms, and processing units. The design and realization of STASIS will account for these.

1.4 Functional Breakdown Structure

Figure 4 shows the generic functional breakdown structure (FBS) for STASIS.
As we can see, the boxes corresponding to the platform itself - marked in grey - are three:

- the Balancing subsystem, which role is to make sure that no gravitational torques act on the platform;
- the Power Generation and Management subsystem (PGMS), whose role is to provide and manage the proper power to every other subsystems on the platform, including the FlatSat representing the CubeSat itself;
- the Attitude Determination and Control Subsystem (ADCS), which role is to provide the control required to the platform in the different simulation phases and estimate the orientation of the platform to provide the data to the orbital propagator (as detailed in Figure 3)

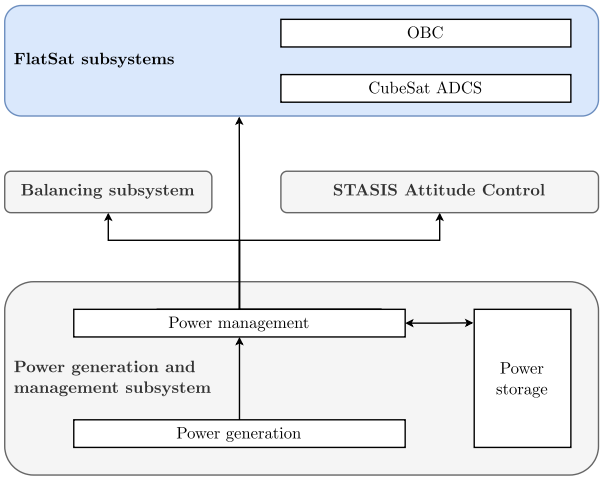

Fig. 4: Summarized FBS of STASIS

Figure 5 shows a rendering of the 3D CAD model of the platform. In the following sections, the main subsystems here introduced will be described in detail, and the design choices that ultimately led to the current design of the platform will be explained.

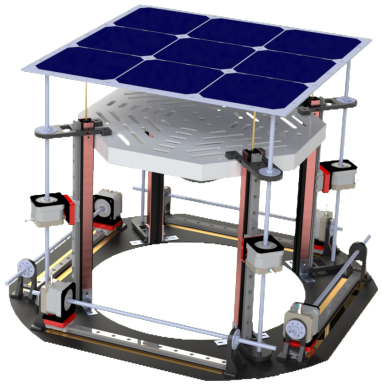

Fig. 5: 3D rendering of STASIS

Copyright © 2022 by Mr. G. Di Domenico. Published by the IAF, with permission and released to the IAF to publish in all forms.

2 Platform Balancing

The core of the attitude simulator is the air-bearing spherical joint. Air bearings have been extensively employed in research and industrial applications to enable frictionless or quasi-frictionless motion around a specific set of degrees of freedom [11]. The working principle of such systems is to create a thin film of air supporting the overlying platform, counter-acting the effect of gravitational forces. For spherical joints, the resulting system is bounded - neglecting the vibrations due to the dynamics of the film of air - to rotate around a fixed point in space, identified by the specific geometry of the air bearing. As Euler's equations for attitude dynamics can be conveniently written around either the center of mass of the object or a fixed point in the inertial space, constraining the platform to rotate around a fixed center of rotation (CR) is a solution to reproduce the attitude motion as it happens in space (where instead the same set of equations are referred to the center of mass (CM) of the object).
However, a major difference between the motion in space and on ground is represented by the effect of gravitational torques on the platform. Indeed, when selecting the CR as reference pole, a term due to the gravitational torques acting on the platform appear in the equations:

$$\mathbf{J}\dot{\boldsymbol{\omega}} = \mathbf{J}\boldsymbol{\omega} \times \boldsymbol{\omega} + m_{\text{tot}}\mathbf{g}_B \times \mathbf{r}_{CM} + \mathbf{M} \tag{1}$$

$\mathbf{J}$	Inertial tensor of the rigid body
$\boldsymbol{\omega}$	Angular velocity vector
m_{tot}	Total mass of the rigid body
$\mathbf{g}_B$	Gravity vector in the reference frame of the rigid body
$\mathbf{r}_{CM}$	CR-to-CM offset
$\mathbf{M}$	External disturbance torques

To remove the effect of the gravitational forces, the platform mass distribution should be such that $\mathbf{r}_{CM} = \mathbf{0}$. In general, two strategies could be employed to achieve this condition. A first strategy is to design the platform such that the condition is intrinsically obtained; this usually requires a high-fidelity CAD model of the platform; this approach can be employed with platforms with a single or a reduced set of configurations. Indeed, any modification could shift the center of mass of the platform, introducing a gravitational torque term and triggering a 3D-pendulum-like motion. The second strategy is instead employed with platform with multiple or flexible configurations: a balancing subsystem - in general represented by a set of moving masses - is foreseen on the platform. Such system works by changing the position of one or multiple balance masses such that the initial CM-to-CR offset is brought to zero. This approach allows a platform to support virtually endless configurations - provided that the control authority of the balancing system is sufficient. A dedicated controller is in charge of the movement of the masses. This is the strategy employed on STASIS: a set of 8 stepper-motor-driven moving masses (two masses along the two in-plane axes and four masses along the vertical direction) is able to carefully control the position of the CM. Such configuration is redundant: the minimum number of masses to achieve the platform balancing is 3. However, the additional degrees of freedom can be used to achieve other peculiar features (e.g., aligning the principal axes of the platform to the axes of the inertial sensors or the ones of the attitude control system).

2.1 Balancing algorithms

Reference [12] reports a survey of existing algorithms for platform balancing. In general, we can distinguish three different approaches:

- an *open-loop* approach relies on the CAD information to properly place the masses and eliminate the gravity torque; however, such approach needs high-fidelity CAD models of every sub-component and is prone to errors;
- an *observe-and-compensate* approach gathers data on the platform motion and estimates the CM-to-CR offset along with the inertial tensor of the platform; the masses are then moved accordingly;
- a *closed-loop* approach, relying on the features of particular moving masses control laws to bring the platform in a particular dynamic state in which the CM-to-CR offset is totally compensated.

Open-loop approaches are useful to gather initial information on the inertial parameters characterizing a specific platform configuration and to evaluate wether the control authority of the balancing subsystem is sufficient to reach a balanced configuration. CAD software are able to automatically return the inertial tensor of the 3D model; however, this requires a comprehensive and accurate modeling of every sub-part of the assembly. This is not always possible (expecially for complex platforms), as not every producer makes the CAD models of every product available to the users; moreover, manufacturing tolerances can introduce errors in the real world that are simply not taken into account in the CAD model. Eventually, non-rigid components (e.g., cables) are difficult to model in a CAD environment.
In EXTREMA, a high-fidelity CAD model for STASIS has been developed as a reference for the accuracy of

Copyright © 2022 by Mr. G. Di Domenico. Published by the IAF, with permission and released to the IAF to publish in all forms.

any other balancing technique. In order to minimize the effect of the above issues, a cable-less design has been carried on. Rigid connections have been preferred over flexible wires, in order to achieve a configuration that was independent from the motion of the platform. To achieve that, Printed Custom Boards (PCB) have been widely employed for the on-board systems. Moreover, rigid rods and rigid sliding connections have been employed for power and data transmission.

The batch observe-and-compensate approach repreents an example of a system parameter estimation problem. By observing the evolution of the platform and exploiting the knowledge of a mathematical model of its dinamycs,it is possible to run optimization algorithms to infer the unknown parameters appearing in the equations. For STASIS, this approach assumes - in its simplest realization - the following 9-element vector as vector of unknown parameters:

$$\boldsymbol{x} = [J_x \; J_y \; J_z \; J_{xy} \; J_{xz} \; J_{yz} \; r_{CM,x} \; r_{CM,y} \; r_{CM,z}]^T \quad (2)$$

The dynamics of the system can be conveniently written as follows:

$$\mathbf{\Omega x} = \mathbf{0} \quad (3)$$

with

$$\mathbf{\Omega}(\dot{\boldsymbol{\omega}}, \boldsymbol{\omega}, \mathbf{g}_b, m_{\text{tot}}) = \begin{bmatrix} \dot{\omega}_x & \omega_x\omega_z & -\omega_x\omega_y \\ -\omega_y\omega_z & \dot{\omega}_y & \omega_x\omega_t \\ \omega_y\omega_z & -\omega_x\omega_z & \dot{\omega}_z \\ \dot{\omega}_y - \omega_x\omega_z & \dot{\omega}_x + \omega_y\omega_z & \omega_x^2 - \omega_y^2 \\ \dot{\omega}_z + \omega_x\omega_y & \omega_z^2 - \omega_x^2 & \dot{\omega}_x - \omega_y\omega_z \\ \omega_y^2 - \omega_z^2 & \dot{\omega}_z - \omega_x\omega_y & \dot{\omega}_y + \omega_x\omega_z \\ 0 & g_{b,z}m_{tot} & -g_{b,y}m_{tot} \\ -g_{b,z}m_{tot} & 0 & g_{b,x}m_{tot} \\ g_{b,y}m_{tot} & -g_{b,x}m_{tot} & 0 \end{bmatrix}^T \quad (4)$$

By collecting multiple samples, it is possible to build a $\mathbf{\Omega}_N$ matrix by appending multiple $\mathbf{\Omega}$ matrices samples at different time instants. The unknown parameters can then be retrieved through a minimum-square approach, solving the following problem:

$$\text{Find } \mathbf{x}^* \text{ such that } \|\mathbf{\Omega}_N\mathbf{x}^*\| \text{ is minimized} \quad (5)$$

However, the above problem allows an infinite number of solutions. Indeed, any scaling $\alpha\mathbf{x}^*$ of the real solution vector $\mathbf{x}^*$ is still a solution of the above problem.

In order to remove the undetermination, a known excitation term must be added to the dynamics. This can be in the form of an explicit control torque (as seen in [13]) or a known shift of the moving masses (similarly to [14]). In the latter case, the equations can be re-written as follows:

$$\mathbf{\Omega x} = \mathbf{k}(\Delta\mathbf{J}, \Delta\mathbf{r_{CM}}) \quad (6)$$

with $\Delta\mathbf{J}$ and $\Delta\mathbf{r}_{CM}$ obtainable by knowing the exact known movement of the masses. The knowledge of $\Delta\mathbf{J}$ and $\Delta\mathbf{r}_{CM}$ is critical to obtain satisfactory results. The above problem is re-formulated as follows:

$$\text{Find } \mathbf{x}^* \text{ such that } \|\mathbf{\Omega}_N\mathbf{x}^* - \mathbf{k}_N\| \text{ is minimized} \quad (7)$$

with $\mathbf{k}_N$ build similarly to the $\mathbf{\Omega}_N$ matrix

A set of initial trials of this approach have been performed with a light version of the platform. A setup as described in Figure 6, with a 9-DoF IMU gathering samples of the angular velocity $\boldsymbol{\omega}$ and an ESP32 microcontroller wirelessly relying data to a MATLAB server, has been made. Instead of the moving masses, a carefully-machined piece was fixed on the platform in different positions. The corresponding $\Delta\mathbf{J}$ and $\Delta\mathbf{r}_{CM}$ have been computed with the aid of the CAD model of the simplified platform. A set of n observation has been performed - each one characterized by a different position of the offset piece. Then, least-square problem of above was solved through MATLAB's `lsqlin` function. The results were compared to the ones of a 3D CAD model; however, these were mostly off the reference values. After careful investigation, the following conclusions have been made:

- a proper knowledge of the dynamics of the system is required. In this case, the absence of a friction term in the dynamics model led to error in estimation. Adding linearly-dependent friction terms required the estimation of the friction coefficient, and resulted in better values for the estimated parameters;
- the presence of moving parts can easily mess up the whole procedure. Indeed, flexible components - whose presence influences both $\mathbf{J}$ and $\mathbf{r}_{CM}$ influence the dynamics of the platform; such influence is greater with the platform being lighter.

According to such considerations, the development of a balancing procedure for STASIS has been postponed to later stages of the project; indeed, the availability of a functional platform - with a precise mass positioning system, a working attitude control system, and an accurate attitude estimation procedure - would open up the possibility to employ better and more complex procedure

Copyright © 2022 by Mr. G. Di Domenico. Published by the IAF, with permission and released to the IAF to publish in all forms.

resulting in lower values for the CR-to-CM offset. Alternative procedures - maybe involving other representations of the system dynamics (e.g., frequency-based) - are to be explored.

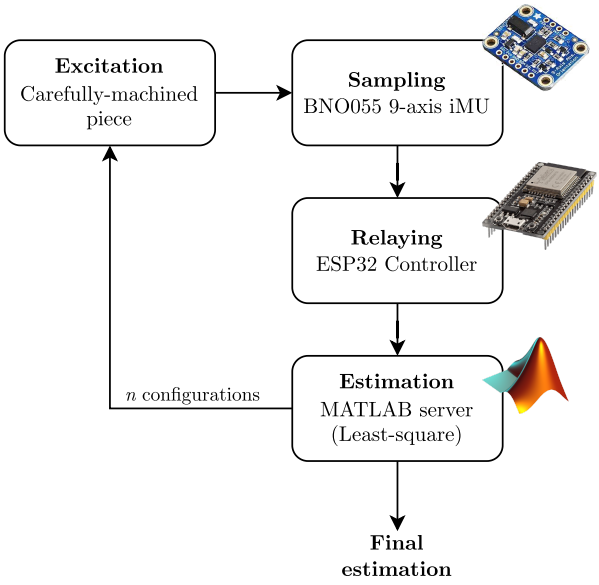

Fig. 6: Schematic of the logic behind the first experiments of the batch estimation procedure.

3 Power Generation and Management

The requirement of minimal external disturbance torques results in additional design challenges for the power generation and management subsystem of STASIS. As previously said, the presence of cables and flexible components on the platform should be minimized in order to achieve an accurate balancing. This implies that either a bulk on-board power storage solution or a wireless power transfer mechanism should be employed. However, despite being accelerated, the duration of the simulations excludes the first option. Indeed, even assuming a 1000-fold acceleration of the orbital dynamics, the simulation of an entire Earth-Mars transfer under continuous low-thrust is expected to last a few days. Assuming an average consumption of 15 W for all the subsystems of more than 650 Wh would be required for a power storage solution. With the typical energy densities of commercially available Li-ion batteries (100-250 Wh/kg, [15]), this would result in a battery pack weight ranging from 2,6 kg to 6,5 kg. Simulation of longer transfers with lighter acceleration factors could easily increas the number to tens of kg of on-board batteries, with serious challenges in terms of balancing and structural design of the platform.

This leaves the implementation of a wireless power transmission system as the only feasible option for longer simulations. Wireless power generation is a topic that has been broadly discussed in literature [16, 17, 18]. However, very few references have been found for wireless power transfer between a fixed source and a rotating target. The surveyed options for STASIS have been:

1. a microwave power generation system, based on an external transmitter and a receiving antenna mounted on the platform;
2. an inductive power generation system, similar to what implemented on modern commercially-available mobile phone wireless chargers;
3. a power beaming solution.

Option (1) has been discarded due to the pointing requirement of traditional antenna and the additional constraint to comply with current safety standards for microwave emissions in human-populated environments[19]; option (2) has been similarly discarded because of the need to keep the coils parallel to maximize the efficiency and the presence of unwanted forces/torques on the platform [20]. Option (3) has been carefully analyzed and a design for such a system has been chosen for STASIS.

Power beaming has received much interest in literature due to the simple design of the components and their availability in the industry. The mechanism is usually associated with light sources in the form of lasers [21, 22], but any light source could work - provided that it is capable to generate enough radiation on top of the receiving array. Such receiving array is made up of a series of photovoltaic devices - solar cells in the simplest case. In [23], a power beaming system reached power transfer efficiency of 68.9%. Lower values - but still significant compared to traditional efficiencies of solar cells - have been obtained multiple times in lab environments [24, 25].

A simple power beaming system is composed of two main sub-components:

1. a light emitting source capable of continuously generating enough radiation;
2. a photovoltaic conversion system able to convert the incoming radiation in electric energy.

While the market enables almost unlimited solutions for what concerns the design of the emitting source, the only feasible options for the photovoltaic conversion system is represented by solar cells.

Copyright © 2022 by Mr. G. Di Domenico. Published by the IAF, with permission and released to the IAF to publish in all forms.

3.1 Power requirement definition

In order to properly size the system, an initial analysis on the power requirements of the platform has been carried on. Without considering reaction wheels - whose dimensioniong is related to the inertia of the platform, and therefore on the solar panel size - the required power has been calculated to be around 15 W in the worst-case condition. This figures includes the power needed to run the sensors, the on-board computing units, and the moving masses[1]

In order to achieve a final power budget, the coupling between the solar array size and the reaction wheels size has been solved. Indeed, a larger surface area for the solar array, while guaranteeing more power under uniform illumination conditions, also requires bigger reaction wheels for a fixed level of attitude control authority. The following table summarizes the nomenclature defined in the following mathematical equations.

J_0	Inertia of the platform around the selected axis of rotatiom, without considering solar array and reaction wheels
J_{RW}	Inertia of a single reaction wheel around the selected axis of rotation
J_{PV}	Inertia of the solar array around the selected axis of rotation
θ	Angular coordinate around the selected axis of rotation
ω	Angular velocity around the selected axis of rotation
$\dot{\omega}$	Angular acceleration around the selected axis of rotation
m_{PV}	Total mass of solar panel
P_{tot}	Total power required for the platform to operate
P_0	Power required for the platform to operate, excluding reaction wheels
P_{RW}	Power required for a single reaction wheel to operate
m_{PV}	Total mass of solar panel
m_{PV}	Total mass of solar panel
η_{RW}	Efficiency of the reaction wheels' DC motor

The reference maneouver for reaction wheels sizing is a single-axis slew maneouver executed with a bang-bang reaction wheel actuation profile, with the wheel rotating in different directions in the accelerating and decelerating phases (Figure 7).

The time limit for the maneouver - 60 minutes for a 270 deg eigenaxis rotation - has been obtained from the requirements of the navigation algorithm under development in EXTREMA. From that, a 20x acceleration has been applied, resulting in a maneouver of 270 deg around a single axis to be completed in 1 minute. From that, the maximum thrust needed has been retrieved:

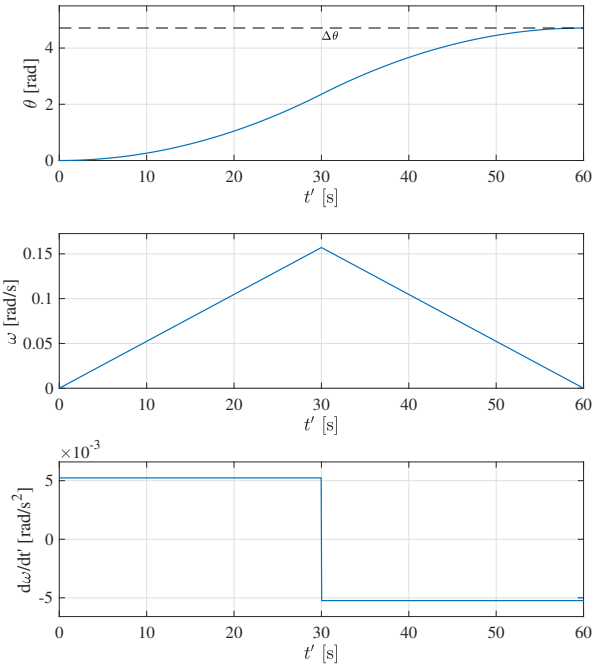

Fig. 7: Evolution of the rotation angle θ, angular speed ω, and angular acceleration $\dot{\omega}$ during the reference maneouver.

$$T = J\dot{\omega} \tag{8}$$

The inertia J of the platform is directly dependent on the size of the solar array and - in minor part - on the size of the reaction wheels themselves. The following formula has been used to explicitly define the single-axis inertia value:

$$J(d, RW) = J_0 + \frac{1}{6} m_{PV} d^2 + 4 \cdot J_{RW} \tag{9}$$

with m_{PV} being the total mass of the solar panel. In order to calculate it, a PV module stack-up made of a 2 mm-thick aluminum sheet and EVA sheet as encapsulant has been assumed. The resulting module aeral density of of 1.7 kg/m^2 has been increased to 2.5 kg/m^2 with a conservative approach. The third equation directly relates the peak power required to operate the reaction wheels to the inertia of the platform and - therefore - to the area of the solar panel. The worst-case condition is when the reaction wheel is close to saturation, because the change in rotational energy to generate the required torque is greater. To further add a safety margin to the dimensioning process, it has been assumed that every reaction wheel is subjected to the same power requirement at the same time. Despite this being not realistic

[1] Despite the moving masses being still during the simulation, power is required for the stepper motors holding torque.

Copyright © 2022 by Mr. G. Di Domenico. Published by the IAF, with permission and released to the IAF to publish in all forms.

- as the reaction wheel configuration is redundant, and because it has been assumed that the maneouver is a single-axis maneouver executed around the maximum-inertia axis of the platform - it is a conservative estimation for the power required to compensate the internal friction between the wheels rotor and the bearing, that would otherwise slow down other wheels triggering undesired rotational dynamics of the platform.

$$P(J_{RW}, d, \text{RPM}) = P_0 + 4 \cdot P_{RW} = \\ = P_0 + 4 \cdot \frac{J(J_{RW}, d)\ \text{RPM[rad]}\ \dot{\omega}_{\max}}{\eta_{RW}} \tag{10}$$

The problem is characterized by 3 degrees of freedom (DoF), since the design is related to the values of the variables d, J_{RW}, and RPM. It can be reduced to a 2-DoF problem by setting the maximum RPM of the reaction wheels' motors. By aligning our design to industrial and commercial standard, conservative values from 500 to 3000 RPM have been selected. These are directly correlated to the maximum momentum storage of the reaction wheels, a crucial parameter to watch out during the execution of the simulation, that can be simply computed as:

$$h_{\max} = J_{RW}\text{RPM[rad]} \tag{11}$$

While the $\Delta\omega$ achievable by the platform before the saturation of the wheel can be obtained as:

$$\omega_{\text{sat}} = \frac{J_{RW}}{J_{\text{tot}}}\text{RPM[rad]} \tag{12}$$

Figure 8 shows the power plots for different values of the solar array size and RPM. The figure also show the corresponding values of the maximum ω achievable by the platform before the saturation of the reaction wheel. The results showed that the original power requirement P_0 is only slightly affected by the presence and activation of the reaction wheels. This is due to the fact that, despite being accelerated, the reference maneouver still requires 60 seconds to be completed, resulting in a power-efficient reaction wheel activation profile. Considering these results, the resulting size for the solar array size has been adapted to the geometry of the platform. A 400x400 mm solar panel has been considered, to be eventually adapted to the available sizes configuration of the employed solar cells. The dimensioning of the reaction wheel will then follow the requirement on the maximum required momentum storage, an output of a more in-depth analysis of the thrust pointing profile and atittude maneouvers required during the mission.

3.2 Emitting-receiver design

The resulting figure of 20 W for the platform power requirement has been referred to when carrying on the design of the emitter and receiver for the power beaming system. The design of the emitter has been carried on with the goal to maximize the conversion efficiency. In order to do that, two main design parameters have been carefully chosen. For what concerns the shape of the beam design, an *illumination efficiency* has been defined as the ratio between the total radiative power emitted from the source and the radiative power impinging on the active surface of the platform. In formulas:

$$\eta_{ill} = \frac{P_{rad,emitted}}{P_{rad,received}} \tag{13}$$

Assuming a point source, the illumination efficiency is directly dependent on the beam angle of the source. If the projected light covers only the active area, the illumination efficiency equals 1. However, even with smaller beam divergence angles (i.e. 15 deg), the resulting illumination efficiency quickly drops. An accurate evaluation of the illumination efficiency of a source requires the knowledge of its antenna function. In order to maximize the energy conversion, two paths have been pursued:

- maximizing the illlumination efficiency by properly shaping the output beam;
- selecting a light spectrum that maximize the conversion efficiency.

A framework to properly compute the produced power for different spectrum and beam spreading functions has been developed, based on a ray-tracing approach.
In order to calculate the efficiency of the solar cells under the provided spectrum, the spectral response of typical c-Si cells has been considered [26]. It is important to note that the spectral responsivity of a solar cell is typically given in [A/W] and referred to the short-circuit current value. Very few references are found in literature reporting the direct dependence of the efficiency of the solar cell (intended as the ratio between the incident power and the output power at the maximum power point) with the radiation wavelength. However, reference [27] reports the variation of the open-circuit voltage of the cell as a function of the incident light spectrum. As the latter is negligible, if also the fill factor (FF) of the solar cell is assumed to be constant with respect to the radiation wavelength, it is possible to state that the $\eta\lambda$ function shares the same trend of the short-circuit current. With such an assumption, one could compute the efficiency of a PV cell under any incoming spectrum as follows. Since the *shape* of the $\eta(\lambda)$ function is known, the normalized spectral efficiency $\overline{\eta}(\lambda)$ can be written as:

Copyright © 2022 by Mr. G. Di Domenico. Published by the IAF, with permission and released to the IAF to publish in all forms.

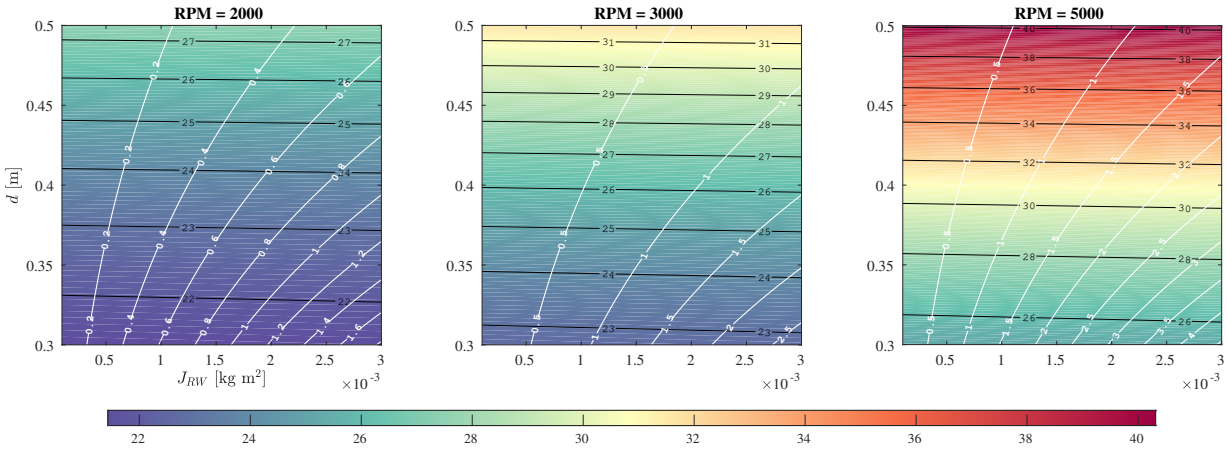

Fig. 8: Contour plots of the required peak power and the resulting maximum momentum storage for different values of the solar panel array size, reaction wheel inertia and maximum BLDC speed.

$$\overline{\eta}(\lambda) = \frac{i_{sc}(\lambda)}{\max_{\lambda\in[0,+\infty]} i_{sc}(\lambda)} \tag{14}$$

with $i_{sc}(\lambda)$ being the spectral responsitivity of the cell as typically defined. Considering an infinitesimal bandwidth of width $d\lambda$ centered at λ_0, the infinitesimal power generated by a source with intensity I_0 and spectrum centerend around λ is:

$$dP = \eta_\lambda(\lambda_0) I(\lambda_0) d\lambda \tag{15}$$

The total power generated by a source with a non-narrow, continuous spectrum is:

$$P = \int_0^\infty \eta(\lambda) I(\lambda) d\lambda \tag{16}$$

The function $\eta(\lambda)$ has the same shape of the normalized spectral responsivity, therefore:

$$P = \int_0^\infty c \cdot \overline{\eta}\lambda I(\lambda) d\lambda = c \int_0^\infty \overline{\eta}(\lambda) I(\lambda) d\lambda \tag{17}$$

Typical PV efficiency values are reported in the manufacturers' datasheet with an efficiency value under 1 Sun of illumination at maximum power point (MPP) condition. As 1 Sun equals a source of light with the same spectrum of the Sun and 1000 W/m^2 of intensity, one could also write:

$$P = \eta_{DS} I_\odot = \eta_{DS} \cdot 1000 \tag{18}$$

with η_{DS} representing the datasheet value for the specific solar cell. If we assume our original source of light having 1000 W/m^2 of efficiency, then:

$$c \int_0^\infty \overline{\eta}(\lambda) I(\lambda) d\lambda = \eta_{DS} I_\odot \tag{19}$$

As all of the values appearing in the previous equation except c are known - being them the normalized spectral efficiency, the Sun light intensity profile, the datasheet efficiency and the total value for the solar flux at 1 Sun - the constant c can be retrieved as:

$$c = \frac{\eta_{ds} I_\odot}{\int_0^\infty \overline{\eta}(\lambda) I(\lambda) d\lambda} \tag{20}$$

Solving for c allows one to compute the efficiency value for any light spectrum at 1 Sun as:

$$\eta(\lambda) = \frac{P}{1000} = \frac{\int_0^\infty \eta(\lambda) I(\lambda) d\lambda}{1000} \tag{21}$$

In general, such procedure is valid only for efficiency for sources at 1000 W/m^2, since the dependence of the solar cell efficiency and maximum power is non-linear with the incoming radiation [28, 29]. However, for irradiance values around the reference condition of 1 Sun, one could assume a linear variation of the output power at the maximum power point with the incoming radiation. Under this simplification, the spectral efficiency can be computed for any source at any intensity:

$$\eta_\lambda = \frac{P}{I_0} = \frac{\int_0^\infty \eta_\lambda(\lambda) I(\lambda) d\lambda}{I_0} \tag{22}$$

And therefore, only the normalized spectrum is needed to compute the spectral efficiency of the cell:

$$\eta_\lambda = \int_0^\infty \eta_\lambda(\lambda) \frac{I(\lambda)}{I_0} d\lambda = \int_0^\infty \eta_\lambda(\lambda) \overline{I}(\lambda) d\lambda \tag{23}$$

Copyright © 2022 by Mr. G. Di Domenico. Published by the IAF, with permission and released to the IAF to publish in all forms.

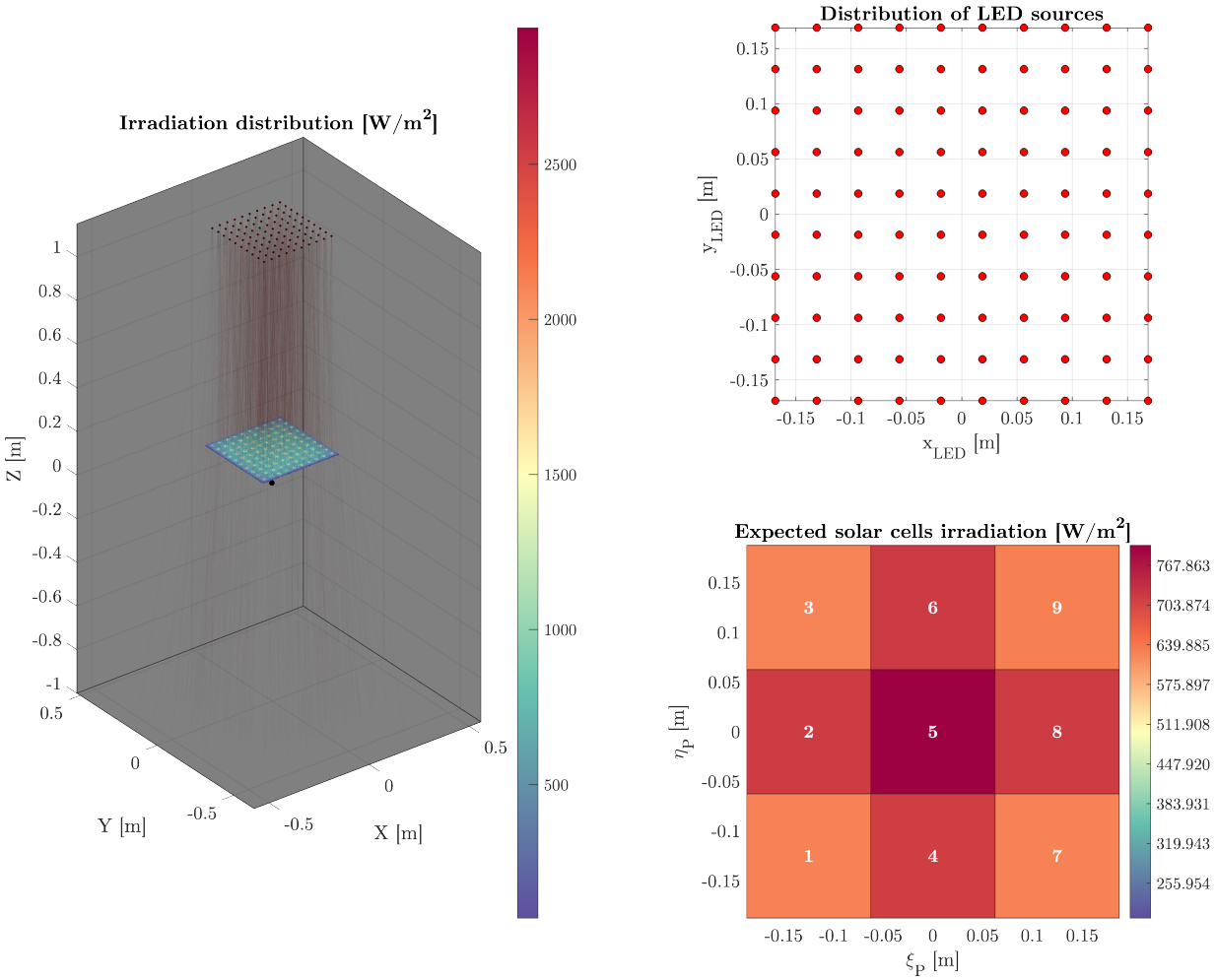

Fig. 9: Simulation output for a flat plate and an array of 10x10 LEDs

For a a gaussian-shaped spectrum centered around 730 nm, a high-efficiency c-Si solar cell with nominal efficiency of 24% results is able to convert the 30% of the incoming power into electrical power at its maximum power point; moreover, red light is way less harsh to the human eye with respect to the full white spectrum at any temperature [30], and red LEDs are also more efficient with respect to other colors [31]. Moreover, as the energy of red photons is closer to the c-Si band-gap energy [32] with respect to other light colors, less energy is dissipated in the solar cell as heat, resulting in better efficiencies during prolonged operations.

Values for the peak photon wavelength for the light source closer to 1000 nm could yeld even higher efficiencies (i.e., 40% for a spectrum centered around 900 nm). However, the market currently offers less solutions for high-power IR leds, and finding datasheets for narrowing optics for such shapes is even more difficult.

Since collimating LED lights is not a trivial task [33], the chosen solution involves an array of LED lights at about 730-800 nm of wavelength with distributed optics. Multiple LEDs and optics from different manufacturers have been simulated. Once the source spectrum and the resulting PV efficiencies have been solved for, the next step involved the selection a proper narrowing optics and geometric distribution of the light sources to maximize the calculated power. To do that, a series of ray-tracing simulation have been developed. Through rejection sampling of the probability density function [34] of the distribution, a set of rays are casted according to the radiation pattern of the source; such rays are then propagated and their possible intersection with the solar array previously designed calculated.

The total emitted power is distributed equally across each ray, and the sum of all the power associated to intersected rays is used to compute the incident power on the solar array. This value is then multiplied with the expected efficiency of the array in order to obtain the expected generated power. Figure 9 shows the output for a 10x10 square LED distribution; such

Copyright © 2022 by Mr. G. Di Domenico. Published by the IAF, with permission and released to the IAF to publish in all forms.

central-symmetric distribution has been chosen in order to exploit small-batch production from high-volume PCB suppliers. The series-connected LED strip is powered through a constant-current LED driver capable of supplying the required current to operate the LEDs at their maximum power output. As the LEDs are energy-intensive, a metal-core PCB has been chosen and a suitable heatsink have been added to the board - providing both thermal relief and structural support. Such a configuration is able to obtain an illumination efficiency of aroun 87%, resulting in a 15% increase in output power from the solar cell (Figure 9). Moreover, with respect to a traditional white spectrum, the increase in output power is even greater, at around 43%.

3.3 Power management

Guaranteeing the optimal light flux and spectrum on the solar array is not sufficient to maximize the power available to the platform. Indeed, it is well-known that solar cells operate under a characteristic curve [35] according to their load resistance. In order to guarantee operation in the nearby of the maximum power point (MPP), a power management system should be deployed.
Moreover, in order to account for shortages and/or insufficient peak power, a backup energy storage system should be envisioned. Both PV array and batteries should work continously and synergically: when the generated power is greater than the power required by the load, the excess power should go into charging the batteries; on the contrary, when the required power is more than the one produced by the solar cells, the batteries should supply enough power to compensate.
The Power Management System (PMS), moreover, should be able to guarantee the correct voltage for the operation of the platform subsystems. These include the brushless DC motors (BLDC) powering the reaction wheels; the inertial sensors, the computing units and the platform balancing system.
A functional schematic of the chosen design can be seen in Figure 10.
As we can see, the power coming from the solar panels is directly converted to the proper voltage needed to charge the batteries and goes through a power path manager that properly dictates wether the power should go into the load or into the batteries - or vice-versa. A power path architecture allows higher load currents and proper current sensing, achieving better performance at peak loads and in terms of safety. Moreover, a set of buck converters is employed to produce three more power lines: a power lines at 9V to power the stepper motors for the balancing system, a power line at 5V to power the computing units and the electronic. As sensors usually require low power levels, additional voltage drops at even lower levels (e.g., 3V3) can be achieved with less-efficient linear regulators.
A doverous note should be added for what concercs the design procedure for the choice of the electronic components for power management. Indeed, the power generation mechanism chosen is subjected to a major difference with respect to traditional solar cells application. Despite the LED-grid solution being able to deliver a low spread angle, artificial, un-collimated light introduce the issue of non-uniform illumination across the panel - expecially at non-flat orientations of the platform (Figure 11).
Such an issue introduces problem with the traditional series-parallel structure of solar arrays. Indeed, when identical cells are connected in series but are subjected to different irradiance levels, the operating curve of the solar panel changes, featuring lower maximum power levels and also local maximum. This poses an additional set of challenges for MPP tracking that are not solvable with traditional, perturbation-based tracking algorithms [36] [37]. The ideal solution involves a distributed MPPT system. A similar application has already been researched in [38]. The challenge here is that traditional PV cells have open-circuit voltages of less than 750mV range [39] and, therefore, boost converters with unoptimal efficiencies must be employed to perform level-shift to usable voltage levels. Despite the market providing tailored components for single-cell MPPT and voltage-boosting (e.g., STMicroelectronics' SPV1040 chip), the development of such a distributed MPPT system was hindered by a global stock shortage of such components. For this reason, the go-to strategy has been to employ a set of series-connected cells, each one with a bypass diode, and to employ a MPPT algorithm with full panel scan.

3.4 Cable management

The power requirements of the paltform can hinder the respect of the inertial requirements of the platform. Indeed, the high number of different subsystems implies that multiple lines and cables are to be included in the platform design. A proper cable management solution should be envisioned. Issues related to bad cable management include cable entangling with moving parts (e.g., moving masses or reaction wheel) and non-constant inertia during the platform motion. It is important to reduce the number of wires to the very minimum and make them as fixed as possible to the platform.
In the realization of STASIS, an even better approach has been pursued. STASIS is tought to be a "wireless" platform, in the sense that power and data are transmit-

Copyright © 2022 by Mr. G. Di Domenico. Published by the IAF, with permission and released to the IAF to publish in all forms.

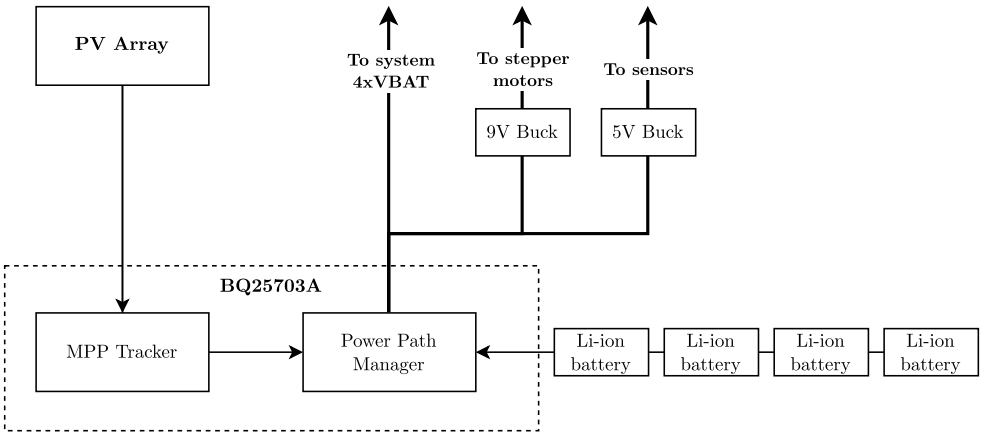

Fig. 10: Functional schematic of the power management system of STASIS

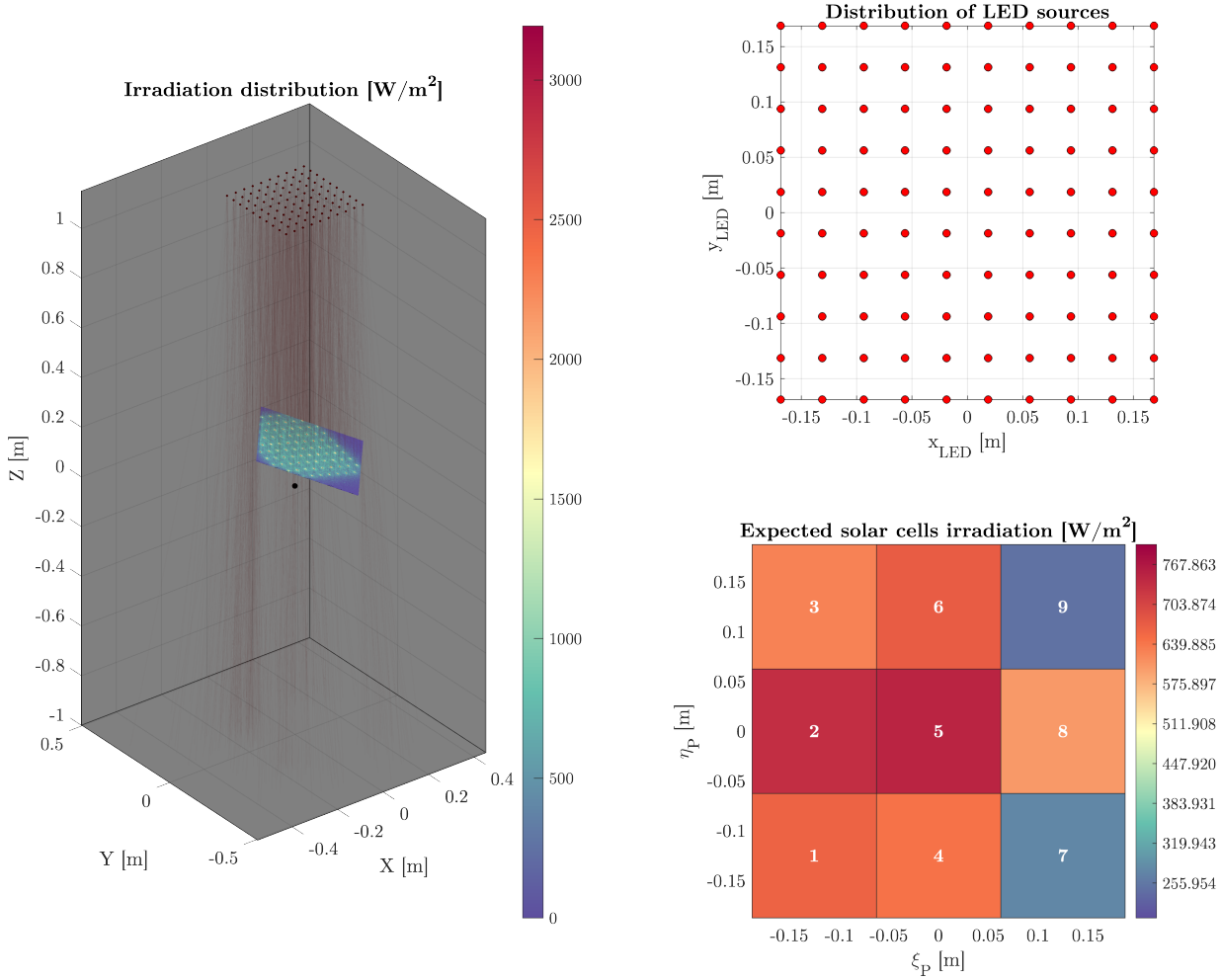

Fig. 11: Non-uniform illumination of different cells on the PV array. The upper-right and lower-right cells receive the lower values of illumination, representing a bottleneck in power generation when connected in series with the other cells.

Copyright © 2022 by Mr. G. Di Domenico. Published by the IAF, with permission and released to the IAF to publish in all forms.

ted without the aid of flexible cables. Multiple design iterations have been carried on with the aim to integrate the structural and power requirements of the platform. The final design - shown in Figure 5, has the following features:

- the positive and negative nodes of the solar panel are connected to the bottom plate through a set of conductive brass screws that fit in the center hole of the structural support beam;
- the batteries and the power management circuit lie on the bottom part of the bottom plate;
- a second pair of threaded rods delivers the VSYS and the 5V0 to the main plate, where the on-board systems are located;
- a set of sliding connections powers the stepper motors controlling the moving masses for balancing
- a custom-designed control board enables the stepper motors to be controlled wirelessly and to directly power the motor coils;

Electronics Design Automation (EDA) practices have been heavily employed to design and produced the required boards and circuitry. Circuit schematics and board design have been carried on through the open-source software KiCad and the production Gerbers files sent to the manufacturers for printing and SMT assembly.

4 Platform Attitude Estimation

The functional schematic for the ESH reported in Figure 3 highlights the need to retrieve the current attitude of the platform to both reconstruct the thruster pointing direction and to determine the portion of the sky to be casted on the optical facility screen (i.e., camera pointing). It is important to understand that such estimation is different from the "internal one": the simulated CubeSat will have its own attitude estimation systems algorithms (e.g., star trackers, IMU, Sun sensors, etc.), with some of them potentially to be tested. Therefore, both the physics, the technology and the requirements of the two attitude estimation requirements are different.
In order for the whole experimental setup to be faithful, the knowledge of the current status of the facilities must be known at the highest possible accuracy, as that would represent the ground-truth for the validation of on-board systems and algorithms. Indeed, it is not possible to know the state of the platform "as-is"; a proper sensing suite - together with filtering and estimation algorithms - should be provided.
The selection of the best methods for attitude estimation usually depend on the employed systems and technology. In the case of STASIS, one should also trade-off between an on-board attitude estimation system, that can be directly attached to the platform and therefore directly infer its attitude, from off-board systems, that measure the environment surrounding the platform to infer its position. The most general realization of an on-board system is an Inertial Measuring Unit (IMU) or a gyroscope; cameras and marker-based systems are instead employed for off-board attitude estimation. It should be noted that, being the simulation a real-time simulation, a second trade-off arises when looking at the estimation frequency and data relaying. Indeed, on-baord systems as IMUs and gyroscopes are able to achieve higher sampling frequencies; this can be critical in the cases of accelerated simulation, as frequencies are scaled down when translated in the simulated system dynamics. However, they require wireless relaying that can introduce additional delays and error in the propagation of the virtualized states. Off-board systems do not suffer from this issue as they can communicate with the main server with cabled connections; however, the employed algorithms are usually more demanding and require higher computational times. Moreover, camera-based off-board systems require high-end hardware to achieve accuracy levels similar to the ones of on-board systems. Still, the main driving factor towards the choice of an off-board system is the fact that they are practically unaffected by bias, differently from gyroscopes. This is particularly critical for long-lasting simulations spanning hours or days. Altough low-bias gyros and bias estimation algorithms exist [40], these usually require the knowledge of a high-fidelity model of the system and therefore can lead to errors in case of non-predictable perturbations. []

4.1 LED-based procedure

In [41], a checkerboard pattern was employed to run a vision-based attitude estimation system. It is common to find approaches employing particular patterns (i.e. ArUco [42]) However, in STASIS it is not possible to employ an extended pattern as the solar cells on the top surface would be covered. An alternative solution is to employ a LED-based attitude reconstruction system, similar to the one employed in [43]. Such a system would work by sensing the position of an array of LEDs and correlate the apparent shape to the known arrangement. Ambiguities due to the symmetry of the platform could be removed by properly exploiting multi-channel information, as for instance different colors for the LEDs.
The current development of the platform did not allow to perform experiment and validation on such technology. However, by exploiting a simple statistical model, it is

Copyright © 2022 by Mr. G. Di Domenico. Published by the IAF, with permission and released to the IAF to publish in all forms.

possible to provide some rough figures for the typical accuracy of such a platform. The underlying assumptions to this procedure are the following:

- each LED is modeled as a point-like source;
- perfect centering of the camera with respect to the platform;
- pinhole model of the camera;
- square camera detector;

If the above are tought to be true, it is possible to state that - for how the pinhole model is conceived - each LED occupies a single pixel on the camera detector. The geometry of the problem - for a rotation of the platform around a single axis parallel to one of the PV array plate side - is reported in Figure 12.
According to this geometry, with the exact knowledge of each LEDs position, it is possible to retrieve the inclination angle through the simple formula:

$$\alpha = \cos^{-1}(\frac{l_{app}}{l}) \tag{24}$$

with l_{app} being the apparent horizontal distance between teh LEDs as sensed by the camera and l the real physical distance between the two LEDs. Such measure, however, is measured with an error that is proportional to the ground resolution g_r of the observing camera. Indeed, the presence of a LED is sensed on the same pixel wherever it is located inside a single resolution cell. In formulas, being $\hat{l}_{app}$ the estimated apparent distance between two LEDs, the estimated angle of the platform will be equal to:

$$\hat{\alpha} = \cos^{-1}\left(\frac{\hat{l}_{app}}{l}\right) \tag{25}$$

To identify the worst-case condition for the estimation procedure, let's assume that the reference length l for the estimation algorithm equals the side of the solar array, previously marked as d - not its diagonal length (being this the greater available reference length on the platform assembly). Indeed, from the previous equation it is clear that the error in $\hat{l}_{app}$ is divided by the reference length. Therefore, the shorter the latter, the higher the error will be.
From the geometry of the problem, it is possible to define a minimum value for the camera field of view (FOV). Indeed, the observation should be such that at every moment the full platform is present in the scene. Assuming a camera-to-CR distance equal to z_C, the minimum FOV is computed as:

$$\mathrm{FOV}_{\min} = 2\tan^{-1}\left(\frac{x_{\max}}{z_C}\right) \tag{26}$$

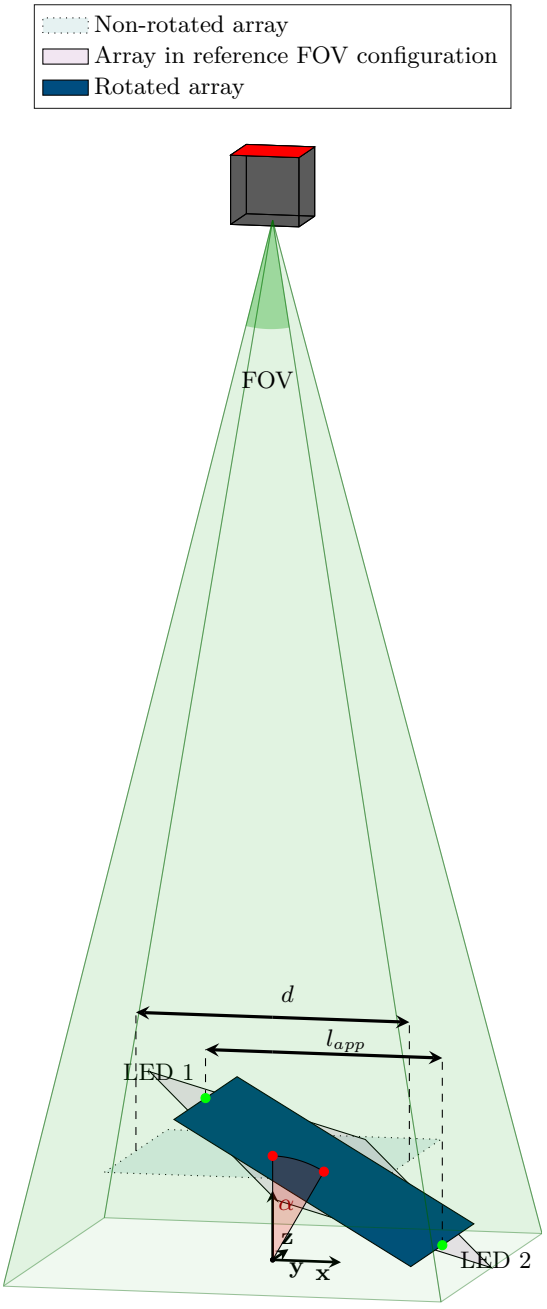

Fig. 12: Geometry of the single-angle attitude estimation problem

Copyright © 2022 by Mr. G. Di Domenico. Published by the IAF, with permission and released to the IAF to publish in all forms.

with $x_{\max}$ being the maximum in-plane distance reached by a point of the platform. In this case, the maximum distance is reached when the full distance from the bearing CR to a corner of the solar array is horizontal. Therefore:

$$\mathrm{FOV}_{\min} = 2\tan^{-1}\left(\frac{d\frac{\sqrt{2}}{2}}{z_C}\right) \tag{27}$$

The position of a LED sensed on a pixel whose centroid is at the normalized detector position ξ_1 cannot be exactly resolved. Indeed, it could be found anywhere in the corresponding ground resolution cell. In one-dimensional terms, the real x-position of the LED is an uniformly-distributed stochastic variables in the $[\overline{x}_1 - \frac{g_r}{2}, \overline{x}_1 + \frac{g_r}{2}]$ interval, with $\overline{x}$ being the physical x-position associated to the pixel centroid, computed as:

$$\overline{x}_i = \xi_i(z_C - z_i)\tan\frac{\mathrm{FOV}}{2} \tag{28}$$

The same applies for a second led with the corresponding pixel centroid at ξ_2. Therefore, the distance between both LEDs is itself a stochastic variable L, with a triangular PDF with mode equal to $\hat{l}_{app} = |\overline{x}_1 - \overline{x}_2|$ and bounded in the $[(\hat{l}_{app} - g_r, \hat{l}_{app} + g_R]$ interval. However, it should be noted that the ground resolution itself is dependent on the z-coordinate of the point, as points at different heights are sensed more or less accurately by the camera. The g_r appearing in the triangular distribution can be written as:

$$\begin{aligned} g_r(\alpha) &= \frac{g_r^+}{2} + \frac{g_r^-}{2} = \\ &= \frac{[1 - z_P\cos(\alpha) - d\sin(\alpha)]\cdot\tan\left(\frac{FOV}{2}\right)}{N_{px}} + \\ &+ \frac{[1 - z_P\cos(\alpha) + d\sin(\alpha)]\cdot\tan\left(\frac{FOV}{2}\right)}{N_{px}} = \\ &= \frac{2[1 - z_P\cos(\alpha)]\cdot\tan\left(\frac{FOV}{2}\right)}{N_{px}} \end{aligned} \tag{29}$$

The last expression is nothing more than the ground resolution expression for the centroid of the solar panel, located at an height of $1 - z_P\cos(\alpha)$ according to the rotation of the solar panel. This means, however, than the resolution of the angular estimation is dependent on the angle itself. By assuming a fixed angle, one can write the expression for the triangular distribution of before:

$$\mathrm{PDF}_L(L) = \begin{cases} 0 & \text{if } |L - \hat{l}| > g_r \\ \frac{1}{g_r}\left(1 - \frac{|L-\hat{l}|}{g_r}\right) & \text{if } |L - \hat{l}| \le g_r \end{cases} \tag{30}$$

The PDF of the stochastic variable representing the estimated angle A can be retrieved by applying the transformation defined by Equation (25):

$$|\mathrm{PDF}_A(A)\mathrm{d}A = \mathrm{PDF}_L(L)\mathrm{d}L \tag{31}$$

one can simply retrieve

$$\mathrm{PDF}(A) = \mathrm{PDF}(L(A))\frac{\mathrm{d}L}{\mathrm{d}A} \tag{32}$$

and therefore

$$\begin{aligned} &\mathrm{PDF}_A(A) = \\ &= \begin{cases} 0 & \text{if } A \notin [\alpha_{\min}, \alpha_{\max}] \\ \frac{d}{g_r} - \frac{d^2\sin(A)\,|\cos(A) - \cos(\hat{\alpha})|}{g_r^2} & \text{if } A \in [\alpha_{\min}, \alpha_{\max}] \end{cases} \end{aligned} \tag{33}$$

with

$$\begin{aligned} \alpha_{\min} &= \cos^{-1}\left(\frac{d\cos(\hat{\alpha}) + g_r}{d}\right) \\ \alpha_{\max} &= \cos^{-1}\left(\frac{d\cos(\hat{\alpha}) - g_r}{d}\right) \end{aligned} \tag{34}$$

The figure to take into account here is the excursion between the $\alpha_{\min}$ and $\alpha_{\max}$ angles, representing - for a single estimation - the error associated to the inclination angle of the platform. As we can see, it is directly dependent on the ground resolution of the platform and, therefore, on the number of pixels N_{px} and the angle itself α of the platform. The expected value of the error changes according to the number of pixel of the detector. Figure 13 reports the expected maximum error associated to an estimation carried on with cameras with different pixel per side.

As we can see, the error decreases with the inclination angle; indeed, despite the ratio between the resolution error and the estimated length increasing, the behavior of the inverse cosine function is such that at higher inclination angles such error has less influence on the angle. On the contrary, when the platform is at an angle close to zero, the estimation is worse when the platform is slightly more inclined. Indeed, since the maximum value for $\hat{l}_{app}$ is bounded to d, the minimum estimated angle α_{min} equals 0, while the maximum estimated angle increases. For a 4k camera (2180p) the error drops below 1 deg at about 7.5 deg of inclination, while it almost reaches 4 deg for lower inclination values. This is

Copyright © 2022 by Mr. G. Di Domenico. Published by the IAF, with permission and released to the IAF to publish in all forms.

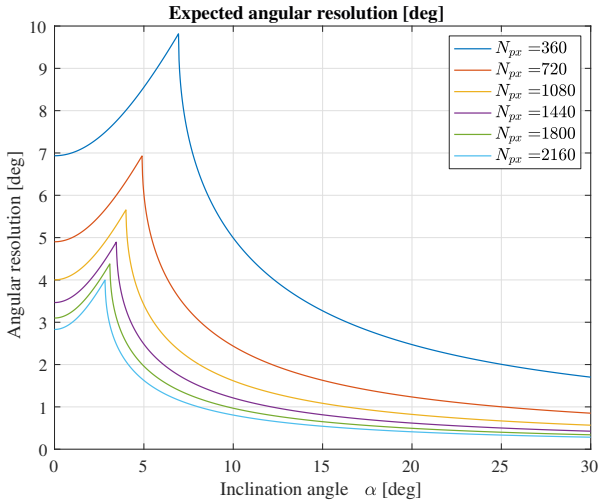

Fig. 13: Angular resolution for different values of the camera pixel resolution and inclination angles

expected, since the cosine function has a slower behavior closer to the zero angle and, therefore, the expected variations are smaller and the effect of the resolution error is more prominent. Moreover, these figures do not take into account additional noise, errors, and manufacturing tolerances, and are expected to be higher in the real world. However, filtering algorithms, multiple camerasm, and tailored acquisition and image processing techniques (e.g., pixel defocusing, which is expected to be able to give sub-pixel accuracies, as described in [10]) should be able to further decrease the indetermination related to a single measurement. Moreover, it is important to stress the need for a proper calibration procedure in order to be able to maximize the accuracy of the estimation procedure.

5 Conclusions

In this work, the current status of the development of the STASIS attitude simulation platform has been presented. The platform has been tought to fulfill the simulation requirements of the EXTREMA Simulation Hub. Particular focus was given with respect to the accuracy of the simulated dynamics, presenting a cable-less design able to minimize the external perturbation with embedded moving masses for optimal balancing. A preevaluation of different balancing algorithm, with an associated experiment, has been performed. However, the techniques tested did not yield good results. In this sense, further research and experiments must be performed, involving a configuration of the platform closer to the final design. The power generation issue has been presented; among the different technologies for wireless power transfer, the power beaming one was selected due to the absence of perturbing torques, the possibility to obtain significant power transfers even with a moving platform, and the design flexibility of the emitter and receiver. The resulting design employs an array of solar cells fed by an external high-power lamp in the far-red wavelength. Such a design - despite having low total efficiency - is able to fulfill the power requirement as estimated by the requirement identification procedure. Eventually, a rough figure for the accuracy of a LED-based attitude estimation system has been given. Further research is needed in order to estimate the effect of the error on the faithfulness of the whole simulation.

5.1 Potential outcomes

Despite STASIS being still in its development phase, it is possible to reason on its potential impact in the current scenario. As of today, CubeSats have been employed mostly on terrestrial orbits; it is therefore not surprising that most of industry and research focused on testing procedure for such applications. As the EXTREMA projects aims to enable autonomous deep-space CubeSats, the need of a platform for comprehensive testing and V&V procedure is needed. In this context, STASIS has to face a set of unique challenges related to the particular target environment and simulation times. The accelerating framework the ESH in based on could represent a breakthrough in this sense - enabling the simulation of entire interplanetary transfers. Once the platform will be operative, it will open the possibility to perform integrated testing of autonomous GNC systems - involving both the attitude and the orbital dynamics - for a wide set of configurations, easing the transition towards a scenario in which swarms of CubeSats will explore the furthest corners of the Solar System in complete autonomy.

Acknowledgments

This project has received funding from the European Research Council (ERC) under the European Union's Horizon 2020 research and innovation programme (grant agreement No. 864697).

Copyright © 2022 by Mr. G. Di Domenico. Published by the IAF, with permission and released to the IAF to publish in all forms.

References

[1] E. Kulu. *Nanosatellites Through 2020 and Beyond*. 2021.

[2] E. Kulu. *Nanosatellite Launch Forecasts-Track Record and Latest Prediction*. 2022.

[3] G. Di Domenico et al. "Toward Self-Driving Interplanetary CubeSats: the ERC-Funded Project EXTREMA". In: *72nd International Astronautical Congress (IAC 2021)*. 2021, pp. 1–11.

[4] A. Morselli et al. "The EXTREMA Orbital Simulation Hub: a Facility for GNC Testing of Autonomous Interplanetary CubeSat". In: *4S Symposium*. 2022, pp. 1–13.

[5] A. Morselli, A. Morelli, and F. Topputo. "ETHILE: A Thruster-in-the-Loop Facility to Enable Autonomous Guidance and Control of Autonomous Interplanetary CubeSats". In: *73rd International Astronautical Congress*. 2022.

[6] A. Bertolino et al. "A survey of field-based testing techniques". In: *ACM Computing Surveys (CSUR)* 54.5 (2021), pp. 1–39.

[7] D. Floreano and R. J. Wood. "Science, technology and the future of small autonomous drones". In: *nature* 521.7553 (2015), pp. 460–466.

[8] M. Wilde, C. Clark, and M. Romano. "Historical survey of kinematic and dynamic spacecraft simulators for laboratory experimentation of on-orbit proximity maneuvers". In: *Progress in Aerospace Sciences* 110 (2019), p. 100552.

[9] G. Di Domenico et al. "The ERC-Funded EXTREMA Project: Achieving Self-Driving Interplanetary CubeSats". In: *Modeling and Optimization in Space Engineering: New Concepts and Approaches*. Springer, 2022.

[10] E. Andreis, V. Franzese, and F. Topputo. "Onboard Orbit Determination for Deep-Space CubeSats". In: *Journal of guidance, control, and dynamics* (2022), pp. 1–14.

[11] J. L. Schwartz, M. A. Peck, and C. D. Hall. "Historical review of air-bearing spacecraft simulators". In: *Journal of Guidance, Control, and Dynamics* 26.4 (2003), pp. 513–522.

[12] R. C. da Silva et al. "A review of balancing methods for satellite simulators". In: *Acta Astronautica* 187 (2021), pp. 537–545.

[13] S. Chesi et al. "Automatic mass balancing of a spacecraft three-axis simulator: Analysis and experimentation". In: *Journal of Guidance, Control, and Dynamics* 37.1 (2014), pp. 197–206.

[14] A. Bahu and D. Modenini. "Automatic mass balancing system for a dynamic CubeSat attitude simulator: development and experimental validation". In: *CEAS Space Journal* 12.4 (2020), pp. 597–611.

[15] J. B. Quinn et al. "Energy density of cylindrical Li-ion cells: a comparison of commercial 18650 to the 21700 cells". In: *Journal of The Electrochemical Society* 165.14 (2018), A3284.

[16] J. L.-W. Li. "Wireless power transmission: State-of-the-arts in technologies and potential applications". In: *Asia-Pacific Microwave Conference 2011*. IEEE. 2011, pp. 86–89.

[17] W. C. Brown. "The history of wireless power transmission". In: *Solar energy* 56.1 (1996), pp. 3–21.

[18] G. A. Landis. "Photovoltaic receivers for laser beamed power in space". In: *Journal of propulsion and power* 9.1 (1993), pp. 105–112.

[19] E. R. Adair and R. C. Petersen. "Biological effects of radiofrequency/microwave radiation". In: *IEEE Transactions on Microwave Theory and Techniques* 50.3 (2002), pp. 953–962.

[20] V.-B. Vu et al. "Operation of Inductive Charging Systems under Misalignment Conditions: A Review for Electric Vehicles". In: *IEEE Transactions on Transportation Electrification* (2022).

[21] D. E. Raible. "High intensity laser power beaming for wireless power transmission". PhD thesis. Cleveland State University, 2008.

[22] V. Andreev et al. "High current density GaAs and GaSb photovoltaic cells for laser power beaming". In: *3rd World Conference onPhotovoltaic Energy Conversion, 2003. Proceedings of*. Vol. 1. IEEE. 2003, pp. 761–764.

[23] H. Helmers et al. "Pushing the boundaries of photovoltaic light to electricity conversion: A GaAs based photonic power converter with 68.9% efficiency". In: *2021 IEEE 48th Photovoltaic Specialists Conference (PVSC)*. IEEE. 2021, pp. 2286–2289.

[24] L. C. Olsen et al. "High efficiency monochromatic GaAs solar cells". In: *The Conference Record of the Twenty-Second IEEE Photovoltaic Specialists Conference-1991*. IEEE. 1991, pp. 419–424.

[25] M. A. Green et al. "45% efficient silicon photovoltaic cell under monochromatic light". In: *IEEE electron device letters* 13.6 (1992), pp. 317–318.

Copyright © 2022 by Mr. G. Di Domenico. Published by the IAF, with permission and released to the IAF to publish in all forms.

[26] N. Reich et al. "Weak light performance and spectral response of different solar cell types". In: *Proc. of the 20th EU PVSEC*. 2005, pp. 2120–2123.

[27] H. Mäckel and A. Cuevas. "The spectral response of the open-circuit voltage: a new characterization tool for solar cells". In: *Solar energy materials and solar cells* 81.2 (2004), pp. 225–237.

[28] M. Chegaar et al. "Effect of illumination intensity on solar cells parameters". In: *Energy Procedia* 36 (2013), pp. 722–729.

[29] M. N. Islam, M. Z. Rahman, and S. M. Mominuzzaman. "The effect of irradiation on different parameters of monocrystalline photovoltaic solar cell". In: *2014 3rd International Conference on the Developments in Renewable Energy Technology (ICDRET)*. IEEE. 2014, pp. 1–6.

[30] J. Schnapf, T. Kraft, and D. Baylor. "Spectral sensitivity of human cone photoreceptors". In: *Nature* 325.6103 (1987), pp. 439–441.

[31] A. M. Muslu et al. "Impact of junction temperature over forward voltage drop for red, blue and green high power light emitting diode chips". In: *2017 16th IEEE Intersociety Conference on Thermal and Thermomechanical Phenomena in Electronic Systems (ITherm)*. IEEE. 2017, pp. 1011–1019.

[32] R. W. Miles, G. Zoppi, and I. Forbes. "Inorganic photovoltaic cells". In: *Materials today* 10.11 (2007), pp. 20–27.

[33] Y.-S. Syu, C.-Y. Wu, and Y.-C. Lee. "Double-sided freeform lens for light collimation of light emitting diodes". In: *Applied Sciences* 9.24 (2019), p. 5452.

[34] B. D. Flury. "Acceptance–rejection sampling made easy". In: *Siam Review* 32.3 (1990), pp. 474–476.

[35] E. Duran et al. "Different methods to obtain the I–V curve of PV modules: A review". In: *2008 33rd IEEE Photovoltaic Specialists Conference*. IEEE. 2008, pp. 1–6.

[36] J. J. Nedumgatt et al. "Perturb and observe MPPT algorithm for solar PV systems-modeling and simulation". In: *2011 Annual IEEE India Conference*. IEEE. 2011, pp. 1–6.

[37] K. Sundareswaran, S. Palani, et al. "Application of a combined particle swarm optimization and perturb and observe method for MPPT in PV systems under partial shading conditions". In: *Renewable Energy* 75 (2015), pp. 308–317.

[38] M. Muthuramalingam and P. Manoharan. "Comparative analysis of distributed MPPT controllers for partially shaded stand alone photovoltaic systems". In: *Energy Conversion and Management* 86 (2014), pp. 286–299.

[39] D. D. Smith et al. "Toward the practical limits of silicon solar cells". In: *IEEE Journal of Photovoltaics* 4.6 (2014), pp. 1465–1469.

[40] J. L. Crassidis, F. L. Markley, and Y. Cheng. "Survey of nonlinear attitude estimation methods". In: *Journal of guidance, control, and dynamics* 30.1 (2007), pp. 12–28.

[41] D. Modenini et al. "A dynamic testbed for nanosatellites attitude verification". In: *Aerospace* 7.3 (2020), p. 31.

[42] C. Vela, G. Fasanogiancarmine, and R. Opromollaroberto. "Pose determination of passively cooperative spacecraft in close proximity using a monocular camera and AruCo markers". In: *Acta Astronautica* (2022).

[43] C. Pirat et al. "Vision based navigation for autonomous cooperative docking of CubeSats". In: *Acta Astronautica* 146 (2018), pp. 418–434.